AIAA JOURNAL
Vol. 45, No. 6, June 2007

Technical Notes

TECHNICAL NOTES are short manuscripts describing new developments or important results of a preliminary nature. These Notes should not exceed 2500 words (where a figure or table counts as 200 words). Following informal review by the Editors, they may be published within a few months of the date of receipt. Style requirements are the same as for regular contributions (see inside back cover).

Shock Detachment Distance on Blunt Bodies in Nonequilibrium Flow

N. Belouaggadia[*]
Hassan II University, Casablanca, Morocco
T. Hashimoto,[†] S. Nonaka,[‡] and K. Takayama[§]
Tohoku University, Sendai 980, Japan
and
R. Brun[¶]
Université de Provence, Marseille, France

DOI: 10.2514/1.17806

Nomenclature

A = chemical symbol
e = total energy per mass unit
e_A, e_D = activation, dissociation energy
e_{Vp} = vibrational energy of species p
$\dot{e}_{Vp}$ = vibrational energy production of species p due to TV and VV collisions
e_{Vps} = vibrational energy gained (lost) by species p due to reaction s
f = distribution function
J = collisional term in Boltzmann equation
K = rate constant
k = Boltzmann constant
$\underline{p}$ = pressure
$\underline{Q}$ = quantity Q at equilibrium
$\boldsymbol{q}$ = total heat flux
$\boldsymbol{q}_v$ = vibrational heat flux
R = hemispherical body radius
T = translation–rotation temperature
T_V = vibration temperature
$\boldsymbol{V}$ = mean velocity (components u and v)
$\boldsymbol{V}_p$ = mean velocity of component p
$\dot{w}_p$ = mass production of species p due to chemical reactions
$\dot{w}_{Vp}$ = vibrational energy production due to chemical reactions
X = longitudinal coordinate in the nozzle
x, y = coordinates in the physical plane
Y = transverse coordinate in the nozzle
Δ = shock standoff distance
Δ/R = normalized shock standoff distance
ρ = density

Subscripts

a, b = upstream, downstream from the detached shock
b = backward reaction
C = chemical
f = forward reaction
i = internal level
p, q = species p, q
R = rotation
s = reaction s
T = translation
TV = translation–vibration exchange
V = vibration
VV = vibration–vibration exchange
ν', ν'' = stoichiometric coefficients
1, 2, 3, 4, 5 = associated to species N_2, O_2, NO, N, O

Introduction

AMONG the aerodynamic quantities sensitive to vibrational and chemical nonequilibrium, the shock detachment distance in front of spherical or hemispherical models is relatively easy to determine from interferometric or Schlieren measurements. Thus, in the past, the experiments performed by Hornung [1] and Wen and Hornung [2] in a shock tunnel and by Lobb [3] in a gun tunnel seem the most significant. More recently, measurements of shock standoff distances in front of hemispherical bodies have been conducted in the ballistic range of the Interdisciplinary Shock Wave Research Center (ISWRC) in the velocity range 2500–4000 km/s [4] and a few others in the free piston shock tunnel (FPST) of ISWRC for enthalpies 4,8 and 10, 4 MJ/kg [5].

Thus, the measurements made in the ballistic range may be correctly, but approximately [6], correlated by the scaling parameter ρR; they also agree reasonably well with values given by an approximate computation using a two-temperature model [4,7] at least for quasi-frozen or quasi-equilibrium conditions; however, in strong nonequilibrium regimes, the computed values underestimate the shock standoff distances [4]. In the same way, the experiments performed in FPST give values close to the frozen case, that is, much larger than those deduced from the two-temperature model. These disagreements seem to come from the important vibrational relaxation connected to a slow chemistry in the ballistic range, and from the freezing of the vibrational temperatures in the freestream at the nozzle exit of the shock tunnel. So a new physical–chemical model must be used, taking these effects into account.

Thus, one of the aims of this paper is to calculate the flow around hemispherical bodies by using the statistical physical–chemical model recently developed by the authors [8,9]; this model, based on a physical analysis, takes into account the vibration–chemistry interaction and so, seems to be particularly adapted to the situations considered here; for the shock tunnel case, the nozzle flow is also computed with the same model.

Modeling and Numerical Simulation

Nonequilibrium Physical Model

In the past, many computations of the hypersonic flow about various models have been developed, first for frozen flow [10], then

---

Received 22 May 2005; revision received 19 January 2007; accepted for publication 12 February 2007.

[*] Assistant Professor, Faculté des Sciences Ben Msik, 7955 Mohamedia.

[†] Graduate Student, Interdisciplinary Shock Wave Research Center.

[‡] Graduate Student, Interdisciplinary Shock Wave Research Center.

[§] Professor, Interdisciplinary Shock Wave Research Center.

[¶] Professor Emeritus, 13170 Les Pennes Mirabeau.

for nonequilibrium flow [2,11–13]; but for situations where the coupling between vibrational and chemical nonequilibrium may be important, new computations are needed. Thus, the physical–chemical model used here for the computation of the hypersonic air flow around hemisphere cylinders has been developed for a dissociating pure gas in [8] and in [9] for a mixture of reacting gases like air.

Thus, considering a reactive gas mixture in a vibrational and chemical nonequilibrium and composed of molecular and atomic species, the Boltzmann equation for the molecules p on a quantum level i, including rotational and vibrational levels, may be written as

$$\frac{df_{ip}}{dt} = J_{TRp} + J_{Vp} + J_{Cp} \tag{1}$$

assuming that the collisional exchanges involving translation–rotation TR, vibration V, and chemical C exchanges, respectively, may proceed on different time scales τ_{TR}, τ_V, and τ_C respectively. For atoms q, we have

$$\frac{df_q}{dt} = J_{Tq} + J_{Cq} \tag{2}$$

The formal expressions of usual macroscopic conservation equations of the mixture are classically deduced from Eqs. (1) and (2) by multiplying the equations by collisional invariants of TR collisions, integrating over velocities and summing over internal levels. In particular, species conservation and vibrational energy relaxation equations can be written as follows:

$$\frac{\partial \rho_p}{\partial t} + \frac{\partial \cdot \rho_p \boldsymbol{u}_p}{\partial \boldsymbol{r}} = \dot{w}_p \tag{3}$$

$$\rho_p \frac{de_{Vp}}{dt} + \frac{\partial \cdot \boldsymbol{q}_{V_p}}{\partial \boldsymbol{r}} = \dot{e}_{Vp} + \dot{w}_{Vp} \tag{4}$$

where $\dot{w}_p$ and $\dot{w}_{Vp}$ are source terms for mass and vibrational energy of species p, respectively, due to reactive collisions.

Equations (3) and (4), coupled with the usual conservation equations of the mixture govern the nonequilibrium phase of the flow. The source terms may be deduced from the set of the s chemical processes of the following type:

$$\sum_p \nu'_{ps} A_p \rightleftarrows \sum_p \nu''_{ps} A_p \tag{5}$$

Thus,

$$\dot{w}_p = \sum_s (\dot{w}_{pfs} - \dot{w}_{pbs}) = \sum_s M_p (\nu''_{ps} - \nu'_{ps})(K_{fs} \Pi N_p^{\nu'_{ps}} - K_{bs} \Pi N_p^{\nu''_{ps}}) \tag{6}$$

$$\dot{w}_{Vp} = \sum_s [(e_{Vp} - e_{Vpfs})\dot{w}_{pfs} - (e_{Vp} - e_{Vpbs})\dot{w}_{pbs}] \tag{7}$$

The expressions K_{fs}, K_{bs}, e_{Vpfs}, and e_{Vpbs} have to be determined to close the complete set of equations, and it is the same for all transport terms appearing in other conservation equations. This may be obtained from a generalized Chapman–Enskog (GCE) procedure [8,14] as follows.

The GCE method consists of expanding f_{ip} in a series of a "small" parameter, here representing the ratio of the vibrational characteristic time to a reference flow time. Excluding the regions where steep gradients prevail, the method applies to nonequilibrium zones up to complete equilibrium; truncating the expansion to the first order, a complete expression of f_{ip} can be obtained and explicit expressions for $\dot{w}_p$ and $\dot{w}_{Vp}$ are found as well as the transport coefficients, pointing out the coupling between vibrational and chemical nonequilibrium. Thus, the rate constants K_s may be written in the following form:

$$K_s = X_s \bar{K}_s \tag{8}$$

with

$$X_s = 1 + \left(\frac{e_{Vp} - \bar{e}_{Vp}}{\bar{e}_{Vp}}\right)\left(\frac{e_{Vps} - \bar{e}_{Vp}}{kT}\right) \tag{9}$$

Details about the method may be found in [8,9], where it is also shown that e_{Vps} may be expressed as a simple function of e_{Dp} or e_{As}, depending on the type of reaction (dissociation or exchange reaction) and on the type of oscillator model. Complete expressions are given in [8,9], as well as applications to simple cases like one-dimensional flows behind a shock wave and boundary layers behind a reflected shock.

For the present case of hypersonic air flow generated in the ballistic range and in the shock tunnel, a mixture of five species (N_2, O_2, NO, O, N) is considered as usual; in the same way, 15 dissociation reactions of the molecular species and 2 exchange reactions involving NO are considered, so that 34 reactions are taken into account, with rate constants given by Eqs. (8) and (9). However, six recombination reactions involving atoms only cannot be described by the present model, which is consistent with the hypothesis, usually assumed, of the independence of these reactions on vibrational distribution of the recombined molecules. Arrhenius rate constants $\bar{K}_s$ are taken from [15] and TV and VV relaxation times from [16,17]. Rather than directly calculating the transport terms, they are written as functions of the viscosity of the mixture and of the nondimensional numbers, namely, frozen Prandtl, Lewis, and vibrational numbers, quantities weakly sensitive to the nonequilibrium [18].

Then, Navier–Stokes equations combined with species conservation equations and with vibrational relaxation equations modified as specified above are solved around the models for the conditions corresponding to the experiments carried out in the gun tunnel. For the case of the shock tunnel experiments, the equations are also solved in the nozzle and then around the models.

Numerical Simulation

In a cylindrical coordinate system (x, y), the unsteady governing equations of a nonequilibrium air mixture, as defined above, may be expressed in the following vectorial form:

$$\frac{\partial \boldsymbol{U}}{\partial t} + \frac{\partial \boldsymbol{F}}{\partial x} + \frac{\partial \boldsymbol{G}}{\partial y} + \boldsymbol{H} = \boldsymbol{\Omega} \tag{10}$$

where the conservative vector $\boldsymbol{U}$ includes the unknown quantities, that is,

$$\boldsymbol{U} = (\rho_1, \ldots \rho_5, \rho u, \rho v, \rho e, \rho_1 e_{V1}, \rho_2 e_{V2})$$

$\boldsymbol{F}$ and $\boldsymbol{G}$ are the vectors including the convective and diffusive fluxes in each direction x and y. The vector $\boldsymbol{H}$ includes the axisymmetrical terms of the equations, and $\boldsymbol{\Omega}$ contains the chemical and vibrational energy source terms.

The unsteady equations (10) have to be integrated around the models and in the shock tunnel nozzle, as specified above, starting from initial conditions and taking into account usual boundary conditions: a time developing solution is so obtained up to the required steady state.

The numerical method is carried out in a rectangular plane ξ, η, derived from the physical plane x, y by a suitable transformation, and the system (10) is solved by an implicit finite difference scheme [11]. For each node (i, j), at the time step $(n + 1)\Delta t$, the system may be written in the following form:

$$\frac{\boldsymbol{U}^{(n+1)} - \boldsymbol{U}^{(n)}}{\Delta t} + \frac{D}{\Delta \xi}(\boldsymbol{F}_e + \boldsymbol{F}_d)^{(n+1)} + \frac{D}{\Delta \eta}(\boldsymbol{G}_e + \boldsymbol{G}_d)^{(n+1)} + \boldsymbol{H}^{(n+1)} = \boldsymbol{\Omega}^{(n+1)} \tag{11}$$

where $\boldsymbol{F}_e$ and $\boldsymbol{G}_e$ represent the Eulerian convective fluxes, $\boldsymbol{F}_d$ and $\boldsymbol{G}_d$ include transport terms, and $\frac{D}{\Delta}$ are finite difference operators.

Each vector $\boldsymbol{\Phi}$ of Eq. (11) is linearized, so that

$$\boldsymbol{\Phi}^{(n+1)} = \boldsymbol{\Phi}^{(n)} + \left(\frac{\partial \boldsymbol{\Phi}}{\partial \boldsymbol{U}}\right)^{n} (\boldsymbol{U}^{(n+1)} - \boldsymbol{U}^{n})$$

where $\partial \boldsymbol{\Phi} / \partial \boldsymbol{U}$ is the Jacobian matrix.

Then, after having split $\boldsymbol{F}_e$ and $\boldsymbol{G}_e$ into a positive and a negative part, the system (11) is written in the following form:

$$\left[\boldsymbol{I} + \Delta t\left(\frac{D_{+}\boldsymbol{A}_{-}}{\Delta\xi} + \frac{D_{-}\boldsymbol{A}_{+}}{\Delta\xi} + \frac{D^{2}\boldsymbol{S}_{d}}{\Delta\xi^{2}} + \frac{D_{+}\boldsymbol{B}_{-}}{\Delta\eta} + \frac{D_{-}\boldsymbol{B}_{+}}{\Delta\eta} + \frac{D^{2}\boldsymbol{R}_{d}}{\Delta\eta^{2}} + \boldsymbol{K} + \boldsymbol{L}\right)\right](\boldsymbol{U}^{(n+1)} - \boldsymbol{U}^{n}) = \Delta \boldsymbol{U}^{(n)}$$

where

$$\Delta \boldsymbol{U}^{(n)} = -\Delta t\left(\frac{D\boldsymbol{F}^{(n)}}{\Delta\xi} + \frac{D\boldsymbol{G}^{(n)}}{\Delta\eta} + \boldsymbol{H}^{(n)} - \boldsymbol{\Omega}^{(n)}\right)$$

D, D_{+}, and D_{-} are, respectively, central, forward, and backward difference operators. $\boldsymbol{A}_{-}$, $\boldsymbol{A}_{+}$, $\boldsymbol{S}_{d}$, $\boldsymbol{B}_{-}$, $\boldsymbol{B}_{+}$, $\boldsymbol{R}_{d}$, $\boldsymbol{K}$, and $\boldsymbol{L}$ are the Jacobian matrices, respectively, of $\boldsymbol{F}_e^{-}, \boldsymbol{F}_e^{+}, \boldsymbol{F}_d, \boldsymbol{G}_e^{-}, \boldsymbol{G}_e^{+}, \boldsymbol{G}_d, \boldsymbol{H}$, and $\boldsymbol{\Omega}$.

After discretization, the system may be written as a pentadiagonal matrix linear system. At each time step, a predictor–corrector scheme is used and the system is solved by a Gauss–Seidel line relaxation method [19] with alternating sweeps in backward and forward direction ξ.

A few thousands grid points are generally required in various meshes (typically 60×80 points), with $\Delta x_{\min} \sim 10^{-5}$ m and $\Delta y_{\min} \sim 10^{-8}$ m. The implicit method enables us to use integration step times Δt increasing from 1 to $10^{3} \Delta t_{\mathrm{CFL}}$. The steady state is obtained after a few thousand iterations.

The shock standoff distance is deduced from these computations in the following way: First, the "numerical thickness" of the shock is estimated by using Prandtl definition, that is,

$$\rho_b - \rho_a \Big/ \left(\frac{\mathrm{d}\rho}{\mathrm{d}x}\right)_{\max}$$

or

$$T_b - T_a \Big/ \left(\frac{\mathrm{d}T}{\mathrm{d}x}\right)_{\max}$$

This thickness may thus be considered as the maximum error made in the shock position, assumed located at the point where the slope of the curves $\rho(x)$ or $T(x)$ is maximum. Finally, considering the numerical results presented thereafter for the gun and the shock tunnel, the maximum error in the shock position is estimated to 5% for the smallest hemispheres.

Experiments

Ballistic Range Experiments

The facility, described in [4] is a two-stage light gas gun: High pressure helium compressed by a piston, accelerated by the combustion of powder rupturing a first diaphragm, breaks a second diaphragm and a projectile accelerated along a 4 m long tube is launched into a 3 m long free flight section (Fig. 1). Particular attention is paid to the purity of the background gas of the test section first evacuated by a molecular pump to 0.1 Pa.

The projectile velocity is measured by pressure ports in the launch tube and shadow and Schlieren techniques are used to visualize the shock standoff distance owing to a Nd-YAG laser of 532 nm wavelength and 5 ns pulse duration, triggered by a pressure transducer. Thus, the relative error caused by the model movement is estimated to be no more than 1% for the highest velocities of the projectile (4000 m/s). The image of the model is recorded in a sheet film sensitive to light in a relatively narrow region of wavelength around 560 nm. The images are magnified and stored in a workstation by using an optical scanner and the shock standoff distance is deduced from the digitized data; including the resolution in reading the shock position, the total average error in the shock standoff distance may be estimated to be less than 5%.

The experimental results are grouped as a function of the scaling parameter ρR. Values of ρR are chosen as 1.10^{-4}, 2.10^{-4}, 4.10^{-4} kg/m^{2} by varying the nose radius from 1 to 15 mm and the initial air pressure from 560 to 20,000 Pa, the velocities of the models (hemisphere cylinders) varying from 2500 to 4000 m/s.

Shock Tunnel Experiments

Measurements of the shock standoff distance are also operated at the exit of the nozzle of the free piston shock tunnel of ISWRC: The facility, as a whole, is described in [5]. It includes a high pressure chamber, a 6 m long compression tube, a shock tube with an inside diameter of 4 cm, a conical nozzle adapted for Mach number of about

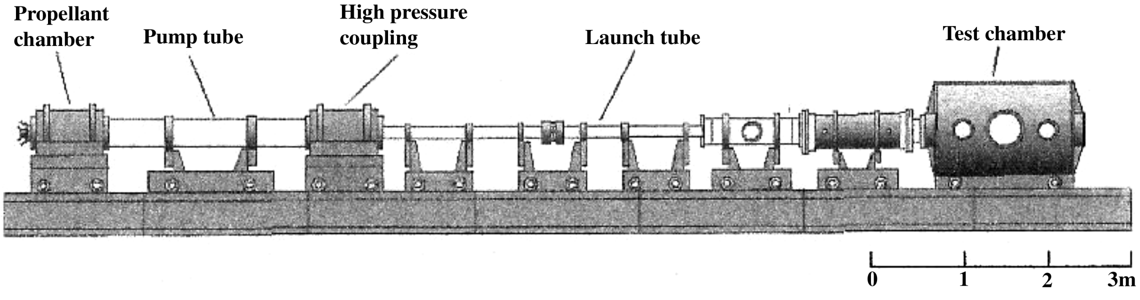

Fig. 1 Scheme of the ballistic range at ISWRC.

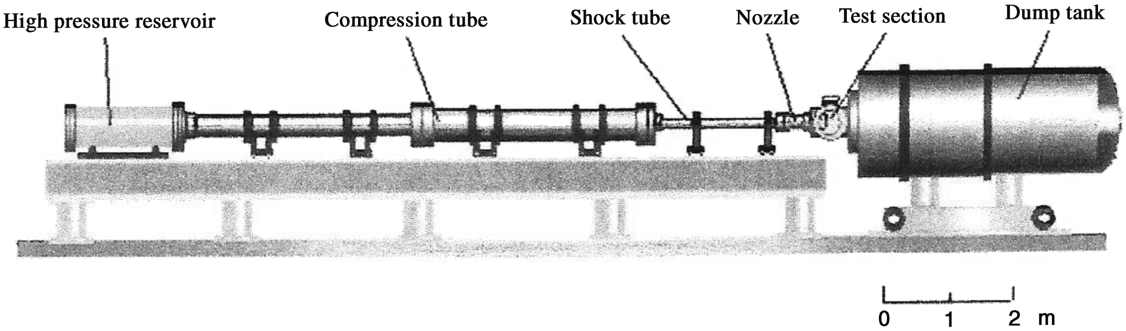

Fig. 2 Scheme of the free piston shock tunnel at ISWRC.

Table 1 Reservoir conditions of the nozzle

Flow quantities		Condition 1	Condition 2
Nozzle reservoir conditions	Pressure, Mpa	18.0	18.0
	Enthalpy, MJ/kg	10.4	4.78
	Temperature, K	6000	3650
Molar concentrations	N_2	0.64	0.75
	O_2	0.06	0.16
	NO	0.15	0.07
	O	0.10	0.02
	N	0.05	0.00

7, a test section, and a dump tank (Fig. 2). The nozzle, attached to the shock tube has a length of 25.7 cm, an exit diameter of 13 cm, and a divergence angle equal to 14 deg. The maximum available total enthalpy is about 15 MJ/kg.

For the present experiments, two reservoir conditions are used (4,8 and 10, 4 MJ/kg), detailed in Table 1. All reservoir quantities are computed from the incident shock velocity measured in the shock tube, assuming equilibrium conditions, but the reservoir pressure is also measured, confirming the computed value. A quasi-steady pressure plateau is observed for about 1 ms with condition 1 and 2.5 ms with condition 2, the difference coming from the nature of the driver gas (He or He/A mixture).

In the same way, the useful test time is determined at the exit of the nozzle with a driver gas detector, sensitive to the specific heat ratio and so, the available test time is found to be about 300 μs for condition 1 and 500 μs for condition 2. Pitot pressure distributions are also performed at 10 and 30 mm from the nozzle exit to test the uniformity of the flow. Thus, an example of the distribution for condition 1 is shown in Fig. 3, where the pressure at $x = 10$ cm is about 65 kPa in a uniform core flow of 55 mm radius. This pressure decreases up to 52 kPa at $x = 30$ mm due to the source flow effect, but at this abscissa, the inviscid flow is about 65 mm wide, which is nearly identical with the nozzle exit diameter. A similar tendency is observed for condition 2.

The optical system used for the flow visualization is a finite fringe holographic interferometry: the light source is a ruby laser of 694.3 nm wavelength with a 25 ns pulse duration and 2 J energy and the shock standoff distance is deduced from the interferograms, so that, as in the case of the gun tunnel, the error made in the determination of this distance may be estimated to be less than 5%.

The hemisphere cylinders used in these experiments have radii of 1.25, 2.5, and 5 cm.

Results and Discussion

Ballistic Range

The measured shock standoff distances, normalized by the nose radius (Δ/R) are plotted in Figs. 4–6. They correspond to ρR values of 1.10^{-4}, 2.10^{-4}, and 4.10^{-4} kg/m^2, respectively. The upper curve represents the well-known solution previously obtained for frozen flow ($\rho R = 0$) and the lower two curves correspond to the equilibrium solution obtained for two different ambient pressures ($\rho R \to \infty$). The domain between these two sets of curves represents the nonequilibrium region for finite ρR values.

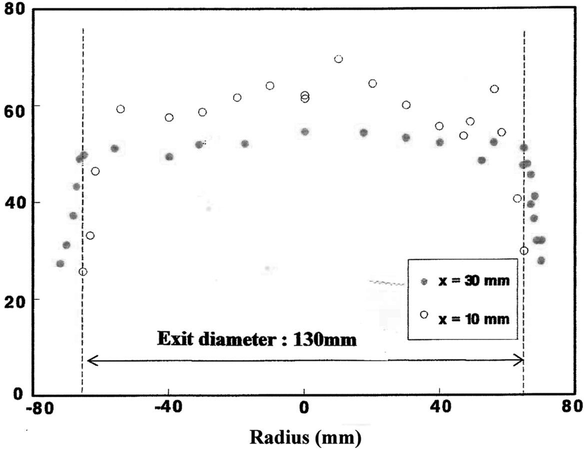

Fig. 3 Experimental Pitot pressure distribution at the exit of the nozzle.

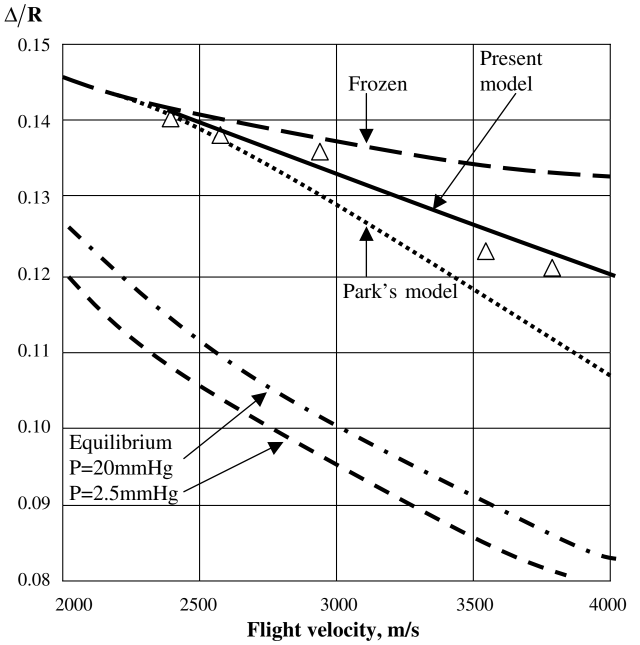

Fig. 4 Comparison between measured and computed shock standoff distance $\rho R = 1.10^{-4}$ kg/m^2; △: experiments.

It is clear that the present experimental data exhibit nonequilibrium effects which become significant when the flight velocity increases while keeping ρR constant; in the same way, as ρR increases, the shock standoff distance approaches equilibrium values.

As previously reported, these results are much closer to the frozen case than older data [3] obtained for similar values of ρR. This discrepancy has been attributed to a contamination of the test gas by oil vapor coming from the oil diffusion pump used in this last case, the organic molecules easily dissociated giving shorter standoff distances.

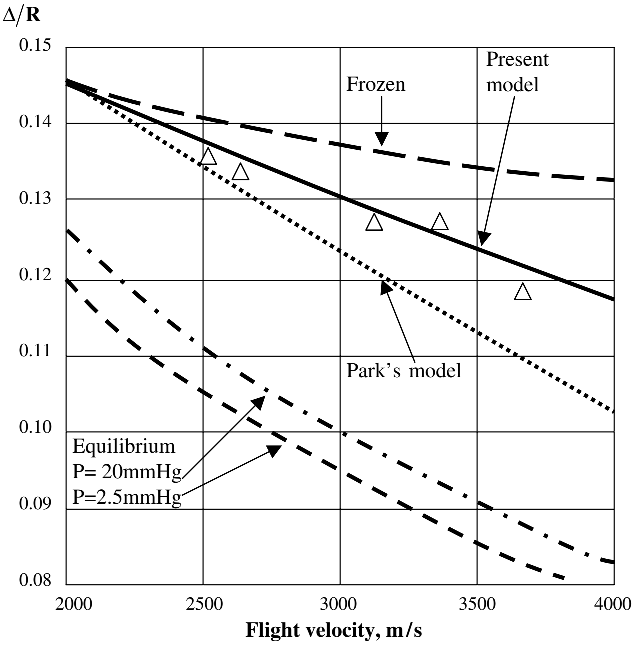

Fig. 5 Comparison between measured and computed shock standoff distance $\rho R = 2.10^{-4}$ kg/m^2; △: experiments.

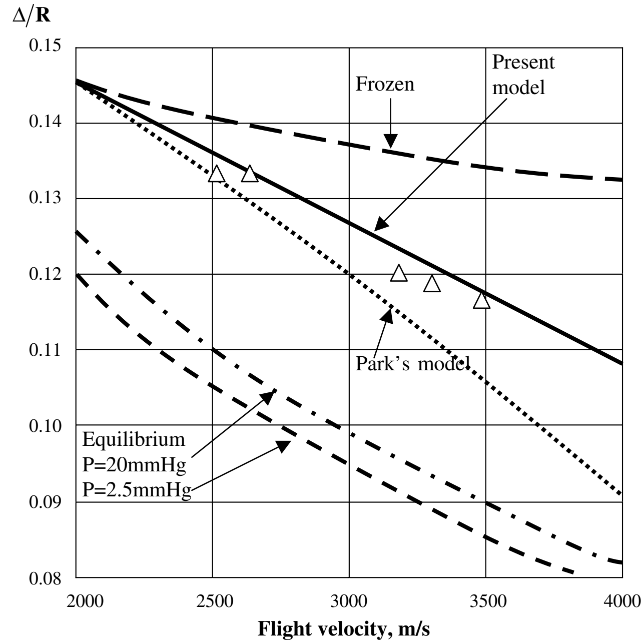

Fig. 6 Comparison between measured and computed shock standoff distance $\rho R = 4.10^{-4}$ kg/m^2; △: experiments.

A comparison with calculations using the two-temperature model derived by Park [7] is also presented in the same figures. As is clearly seen, a fair agreement is obtained for nearly frozen flows (low ρR values, low velocities); it is also expected that the agreement is good in nearly equilibrium conditions. However, the computed values gradually depart from the experimental ones as the flight velocity increases in the nonequilibrium regime and underestimates the shock standoff distance. This may be attributed to a relatively slow chemistry associated with an important vibrational relaxation.

Thus, the present theoretical model taking this coupling into account gives values for the shock standoff distance in good agreement with experimental data in the whole nonequilibrium regime for the three values of ρR. The discrepancies are smaller than 2%, except for one single case (4%).

Shock Tunnel

The values of the main quantities obtained with the present model at the exit of the nozzle (central part) are given in Table 2 for conditions 1 and 2. In the same way, examples of axial profiles of temperatures and species concentrations computed along the nozzle are given in Figs. 7 and 8 respectively. As expected, a typical freezing is clearly visible for concentrations and temperatures at a few centimeters from the throat.

To validate the computation as far as possible, Pitot pressure distribution at the exit of the nozzle has also been computed and compared with the experimental distribution. A fair agreement may be observed in Fig. 9 especially close to the axis of the nozzle, although the computed values slightly overestimate the pressure (5–6%) in the core flow. The experimental and computed boundary layer thicknesses are quite comparable, which is corroborated by Fig. 10, where computed transverse profiles of temperatures at the exit of the nozzle are represented.

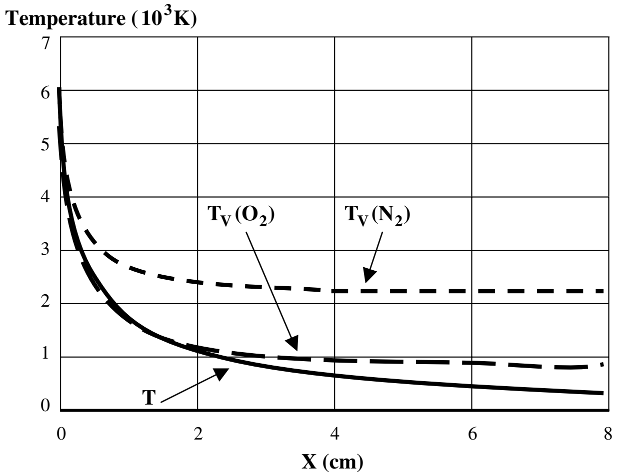

Fig. 7 Axial temperature profiles along the nozzle (condition 1).

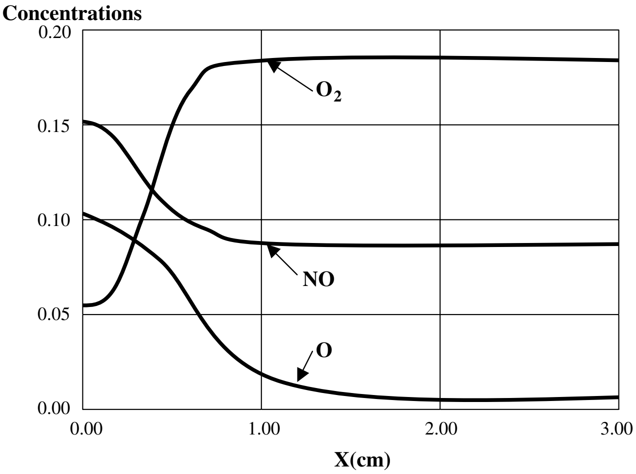

Fig. 8 Axial mole fraction profiles along the nozzle (condition 1).

Table 2 Flow conditions at the nozzle exit (computed)

Flow quantities		Condition 1	Condition 2
Nozzle exit conditions	Mach number	7.25	6.89
	Velocity, m/s	4120	2780
	Temperature, K	420	310
	T_V (N_2)	2120	1900
	T_V (O_2)	900	800
Molar concentrations	N_2	0.73	0.70
	O_2	0.18	0.13
	NO	0.08	0.13
	O	0.01	0.04
	N	0.00	0.00

Then, using the freestream conditions of Table 2, the computation of the flow around the hemisphere cylinders is performed and an example of the evolution of the temperatures along the stagnation line is represented in Fig. 11. It is clear that the nonequilibrium effects in the flow around the body are strongly reduced because of the freezing of these quantities at a rather high level in the freestream of the nozzle. It is the same of course for the evolution of the species concentrations.

The shock detachment distances are deduced from the above calculations and comparisons with corresponding values determined

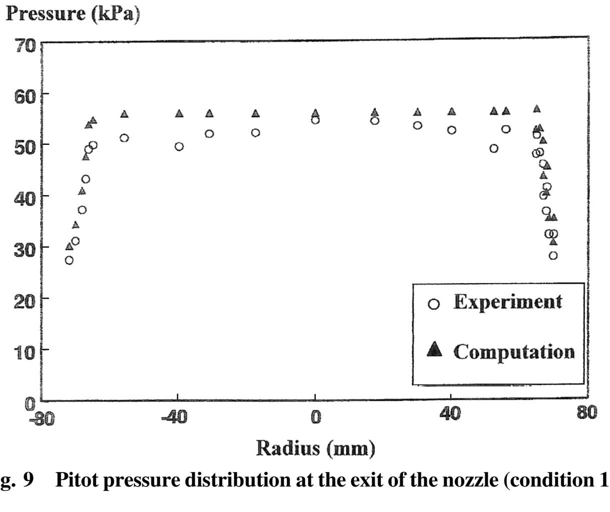

Fig. 9 Pitot pressure distribution at the exit of the nozzle (condition 1).

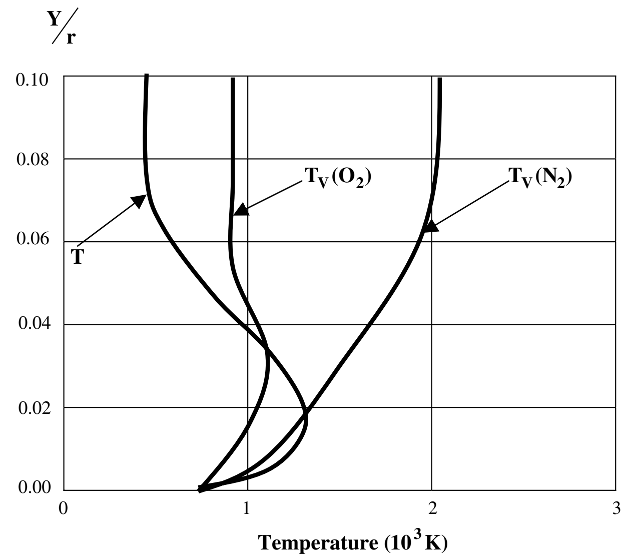

Fig. 10 Transverse temperature profiles at the exit of the nozzle (condition 1).

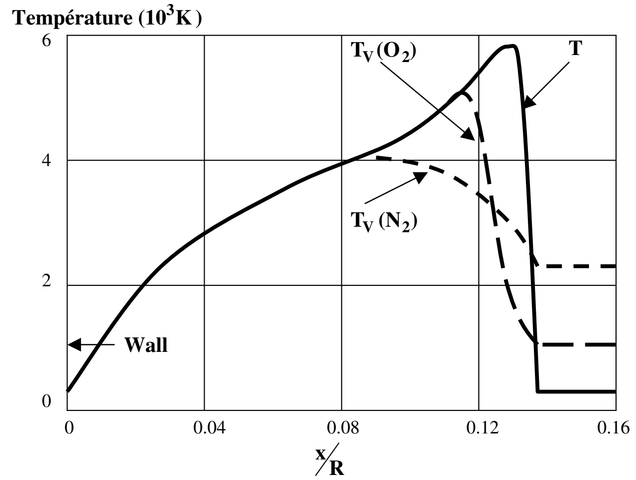

Fig. 11 Temperature profiles along the stagnation line (condition 1).

by interferometry are reported in Table 3. The agreement is rather fair because the discrepancies are about 2–5%, which corresponds to the experimental uncertainties; the maximum discrepancy is observed for the largest sphere radius (5 cm). In this case, interactions between the detached shock and the nozzle boundary layer are not to be excluded. Source flow effects could also be considered, but at high Mach number in a quasi-frozen flow, as is the case here, these effects have a negligible influence on the shock standoff distance.

Finally, comparing the present values to those of the frozen case, only a difference of the order of 10% is observed and the shock standoff distance does not depend significantly on the chemical conditions (1 or 2), this also being due to the high Mach number and quasi-frozen free flow.

On the other hand, as in the case of the ballistic range, the two-temperature model underestimates this distance from about 10%, which is larger than the uncertainty in the measurements and in the present computations (5%).

Table 3 Shock standoff distances in shock tunnel

	R, mm	Δ/R, frozen	Δ/R, computed	Δ/R, measured
Condition 1	25	0.139	0.131	0.129
	50	0.139	0.125	0.121
Condition 2	12.5	0.138	0.130	0.136
	25	0.138	0.127	0.130
	50	0.138	0.124	0.120

Conclusions

Improvements may still be brought to the computation of nonequilibrium flows in nozzles and around bodies, particularly by improving the physical–chemical model itself which could more accurately take the vibration–recombination phenomena into account. A more detailed description of the freestream nozzle flow in front of the body could also be used. However, considering maximum errors in computation and in experiments (5%), the present computed results seem satisfactory in comparison with the experimental data obtained in gun and shock tunnels, thus validating the physical model used in the computations.

References

[1] Hornung, H. G., “Non-Equilibrium Dissociation Nitrogen Flow Over Spheres and Circular Cylinders,” *Journal of Fluid Mechanics*, Vol. 53, 1972, pp. 149–176.

[2] Wen, C. Y., and Hornung, H. G., “Nonequilibrium Dissociating Flow over Spheres,” *Journal of Fluid Mechanics*, Vol. 299, 1995, pp. 389–405.

[3] Lobb, R. K., “Experimental Measurement of Shock Detachment Distance on Spheres Fired in Air at Hypervelocities,” *The High Temperature Aspects of HypersonicFlow*, edited by W. C. Nelson, Pergamon Press, New York, 1964, pp. 519–527.

[4] Furudate, M., Nonaka, S., and Sawada, K., “Behavior of Two Temperature Model in Intermediate Hypersonic Regime,” *Journal of Thermophysics and Heat Transfer*, Vol. 13, Oct.–Dec. 1999, pp. 424–430.

[5] Hashimoto, T., “Analytical and Experimental Study of Hypersonic Nozzle Flows in Free Piston Shock Tunnel,” Ph.D. Thesis, A0TD1606, Tohoku University, Sendai, Japan, 2003.

[6] Anderson, J. D., Jr., *Hypersonic and High Temperature Gas Dynamics*, McGraw–Hill, New York, 1989.

[7] Park, C., “Assessment of Two Temperature Kinetic Model for Ionizing Air,” *Journal of Thermophysics and Heat Transfer*, Vol. 3, April–June 1989, pp. 233–244.

[8] Belouaggadia, N., and Brun, R., “Chemical Rate Constants in Nonequilibrium Flows,” *Journal of Thermophysics and Heat Transfer*, Vol. 12, Oct. –Dec. 1998, pp. 482–488.

[9] Belouaggadia, N., and Brun, R., “Statistical Model for Vibration-Chemical Reaction Interaction: Extension to Gas Mixtures,” *Journal of Thermophysics and Heat Transfer*, Vol. 20, Jan. –March 2006, pp. 148–150.

[10] Hayes, W. D., and Probstein, R. F., *Hypersonic Flow Theory*, Academic Press, New York, 1959.

[11] Candler, G. V., “The Computation of Weakly Ionised Hypersonic Flows in Thermochemical Nonequilibrium,” Ph.D. Thesis, Stanford University, Stanford, CA, 1988.

[12] Klomfass, A., Müller, S., and Ballmann, J., “Analysis of Nonequilibrium, Hypersonic Blunt Body Flow with the Local Similarity Method,” *Shock Waves I*, World Scientific, Singapore, 1996, pp. 741–747.

[13] William, J., “Etude des Processus Physico-Chimiques dans les Écoulements Détendus à Haute Enthalpie: Application à la Soufflerie à arc F4,” Thèse de Doctorat, Université de Provence, Marseille, France, 1999.

[14] Kogan, M. N., Galkin, V. S., and Makashev, N. K., “Generalised Chapman-Enskog Method: Derivation of the Nonequilibrium Gasdynamics Equations,” *Rarefied Gas Dynamics*, edited by R. Campargue, CEA, Paris, 1979, pp. 693–734.

[15] Park, C., “A Review of Reaction Rates in High Temperature Air,” AIAA Paper 89-7740, 1989.

[16] Millikan, R. C., and White, D. R., “Systematics of Vibrational Relaxation,” *Journal of Chemical Physics*, Vol. 39, No. 12, 1969, pp. 3209–3213.

[17] Stupochenko, Y. V., Losev, S. A., and Osipov, A. I., *Relaxation in Shock Waves*, Springer–Verlag, Berlin, 1967, pp. 313–322.

[18] Brun, R., “Transport Properties in Reactive Gas Flows,” AIAA Paper 88-2655, June 1988.

[19] MacCormack, R. W., and Candler, G., “The Solution of the Navier Stokes Equations Gauss-Seidel Line Relaxation,” *Computers and Fluids*, Vol. 17, 1989, pp. 135–155.

G. Candler
Associate Editor